# Design and Fabrication of $S_0$ Lamb-Wave Thin-Film Lithium Niobate Micromechanical Resonators

Renyuan Wang, *Student Member, IEEE,* Sunil A. Bhave, *Senior Member, IEEE,* and Kushal Bhattacharjee, *Senior Member, IEEE*

***Abstract*— Commercial markets desire integrated multifrequency band-select duplexer and diplexer filters with a wide fractional bandwidth and steep roll-off to satisfy the ever-increasing demand for spectrum. In this paper, we discuss the fabrication and design of lithium niobate (LN) thin-film $S_0$ Lamb-wave resonators on a piezoelectric-on-piezoelectric platform. Filters using these resonators have the potential to fulfill all the above requirements. In particular, we demonstrated one-port high-order $S_0$ Lamb-wave resonators with resonant frequencies from ∼400 MHz to ∼1 GHz on a black rotated y-136 cut LN thin film. The effective electromechanical coupling factor ($k_{eff}^2$) ranges from 7% to 12%, while the measured quality factor ranges from 600 to 3300. The highest $k_{eff}^2 \times Q$ achieved on this chip is 194, significantly surpassing contour mode resonators manufactured in other technologies. [2014-0280]**

***Index Terms*— Lamb wave, laterally vibrating resonators, piezoelectric, lithium niobate, quality factor, electro-mechanical coupling factor, TCF, wideband RF filtering.**

## I. Introduction

WHILE HIGH-Q, narrow bandwidth "channel"-select filter arrays are actively pursued for defense applications, commercial markets demand multi-frequency "band"-select duplexer and diplexer filters with fractional bandwidth (BW) ranging from 3% to 10%. For example, a high-end smartphone needs band-pass filters for 2G, 3G and 4G wireless bands, as well as Wi-Fi, Bluetooth and GPS. Therefore a single chip integration solution of filters for all these bands is highly desired. In the past decade, MEMS FBAR (film bulk acoustic resonator) filters and SAW (surface acoustic wave) filters have dominated the duplexer and diplexer market. Such filters consist of a ladder network of multiple MEMS resonators or SAW resonators. The achievable bandwidth of such filter is ultimately limited by the effective electro-mechanical coupling factor ($k_{eff}^2$) of the resonators, while the roll-off is determined by resonator $Q$. The insertion loss is related to resonator motional impedance, which is inversely proportional to $k_{eff}^2 \times Q$. Therefore, to achieve wide BW, high stop-band-rejection, and low insertion loss band-pass filters, resonators with both high $k_{eff}^2$ and high $Q$ are desired.

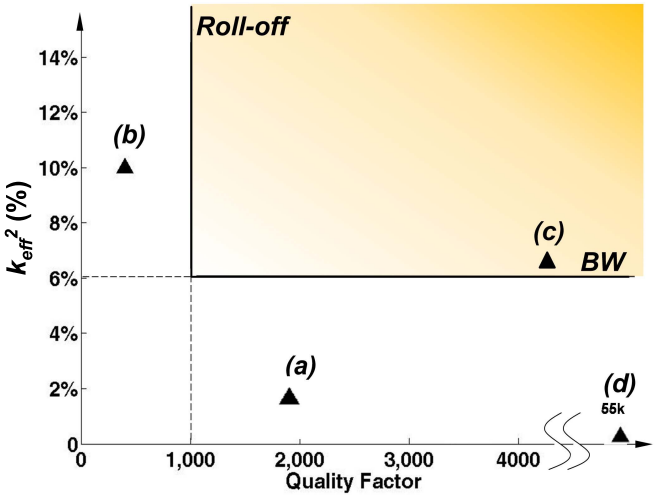


Fig. 1. $k_{eff}^2$ vs. $Q$ of MEMS resonators from different technologies, where the yellow shaded area marks the targeted opportunity and design space for LN Lamb wave resonators. (a) G. Piazza, AlN contour-mode resonator; (b) M. Kadota, SAW resonator; (c) R. Ruby, AlN FBAR; (d) C. Nguyen, diamond disk with electrostatic drive.

Traditional electrostatic drive MEMS resonators have shown very high $Q$ [1], but suffer from extremely low $k_{eff}^2$, due to the poor transduction efficiency of the electrostatic actuator (Fig. 1). Filters using aluminum nitride (AlN) FBARs have demonstrated 7% BW [2] , however it is not suitable for multi-frequency integration as the resonant frequency is determined by the thickness of the AlN thin-film. On the other hand, their multi-frequency contour-mode counterparts have shown very high $f \times Q$ [3], but their $k_{eff}^2$ are limited to <2.5% [4] due to the poor vertical-to-lateral transduction efficiency of sputtered AlN. Consequently, while FBAR filters have dominated the code-division-multiple-access (CDMA) market, filters based on contour-mode AlN resonators have struggled to find a firm footing. Lithium niobate (LN) based SAW filters have shown very large $k_{eff}^2$ and BW [5]. But due to the 1D acoustic energy confinement in SAW configuration, energy is easily dissipated in the transverse direction as well as vertically thru the substrate, which leads to low $Q$ and parasitic modes.

To leverage the high coupling coefficient of LN with the high quality factor from mode-isolation and energy trapping of released and undercut mechanical structures,

Manuscript received September 16, 2014; revised December 12, 2014; accepted December 17, 2014. Date of publication January 9, 2015; date of current version March 31, 2015. This work was supported in part by the Defense Advanced Research Projects Agency through the Adaptive RF Technology Program, and in part by the National Science Foundation under Grant ECCS-0335765, which was performed at the Cornell NanoScale Facility, a member of the National Nanotechnology Infrastructure Network. Subject Editor C. T.-C. Nguyen.

R. Wang and S. A. Bhave are with the School of Electrical and Computer Engineering, Cornell University, Ithaca, NY 14850 USA (e-mail: rw364@cornell.edu; sunil@ece.cornell.edu).

K. Bhattacharjee is with RF Micro Devices, Inc., Greensboro, NC 27409 USA (e-mail: kbhattacharjee@rfmd.com).

Color versions of one or more of the figures in this paper are available online at http://ieeexplore.ieee.org.

Digital Object Identifier 10.1109/JMEMS.2014.2384916

1057-7157 © 2015 IEEE. Personal use is permitted, but republication/redistribution requires IEEE permission.
See http://www.ieee.org/publications_standards/publications/rights/index.html for more information.

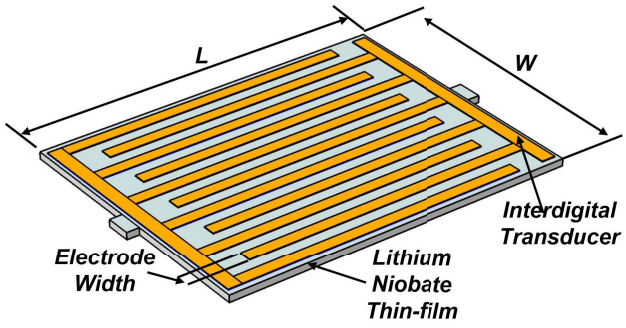


Fig. 2. Conceptual schematic of lithium niobate thin-film $S_0$ Lamb wave resonator.

laterally-vibrating LN thin-film resonators (Fig. 2) have been proposed by our group [6], the Sandia group [7], and the CMU group [8]. The resonant frequency of such devices are primarily defined by their lateral dimension, which can be accurately controlled by photolithography. In this paper, we present a comprehensive study of thin-film LN symmetric $0^{th}$ ($S_0$) order Lamb wave resonators [9] with latest results of these device. We demonstrate resonators with $Q$ ranging from few hundred to over three thousand and having $k^2_{eff}$ of $3\% \sim 12\%$.

We start by introducing our fabrication process of the thin-film LN resonators, then we discuss the design and modeling of these device with emphasis on the importance of interdigital transducer (IDT) positioning. In the next section, we present the experimental result on the loss mechanisms limiting the quality factor and verification of our design methodology. We finally summarize our work and conclude the paper.

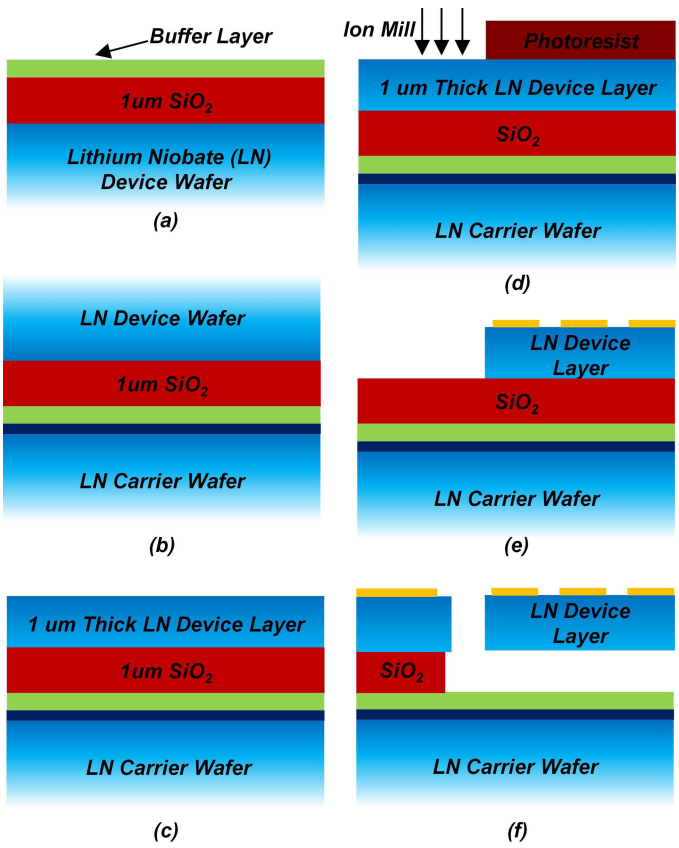


Fig. 3. Fabrication process of lithium niobate thin-film $S_0$ Lamb wave mode resonators: (a) Deposition of sacrificial layer and buffer layer on device wafer; (b) Bonding of device wafer to carrier wafer; (c) Grinding the device layer to desired thickness; (d) Ion-mill defining device geometry using photoresist mask; (e) Lift-off top electrode; (f) Release device in BOE 6:1.

## II. Fabrication

The semiconductor industry traditionally uses epitaxially deposited high quality thin films for the device layer. Many epitaxy growth methods [10]–[13] have been investigated for LN deposition. However high quality single crystal LN-film is yet to be demonstrated. Consequently, researchers generally rely on ion-slicing methods [7], [8], [14]. But the high energy ions used for slicing the thin-film may degrade the thin-film quality. In addition, the stress resulting from the annealing process for recovering the quality of the thin-film, and the thermal mismatch between thin-film and handle wafer can cause thermal instability in the fabricated resonators. This makes it very challenging to fabricate tether suspended free-standing thin-film devices. To mitigate these issues, we use a bonding and thinning process to prepare our LN thin-film, where each step of the process is performed at close to room temperature. Meanwhile, the device wafer and carrier wafer have the same crystal cut, and the crystal orientations are aligned during the bonding to ensure the whole stack expands and contracts in the same way under thermal cycling. This allows us to choose a LN thin-film crystal orientation and layer stack optimized for Lamb wave mode operation, while attaining a thin film with bulk LN single crystal quality.

We performed preliminary search for crystal orientation that provides high coupling factor for $S_0$ Lamb wave modes, and chose to use rotated y-136 cut LN crystal. We start with a rotated y-136 cut LN device wafer deposited with PECVD $SiO_2$ sacrificial layer and a buffer layer to protect the bonding agent from buffered oxide etchant (BOE) during release (Fig. 3). The wafer is then flip-bonded to the LN carrier wafer using glue, and ground down to 1um thickness. Traditionally, reactive ion etching (RIE) is used for anisotropic etching of LN [8], [15], where metal or oxide hard mask and very high RF power are used. However, it is very hard to achieve $>80$ degrees side-wall verticality due to the re-deposition of lithium compound [16]. RIE also tends to exhibit crystal orientation dependent etch rates. Therefore, ion milling is used here to define device geometry with photoresist mask. With an optimized recipe, an angled ion mill etching produces a smooth side-wall with slope close to 90 degrees (Fig. 4), which is crucial to reduce scattering loss of the acoustic wave at the mechanical boundaries. The milling process uses a 4 inch diameter argon ion beam, and the etch rate for LN is 42nm/min. Thus, the process is viable for full wafer scale mass production. The photoresist mask develops a tapered profile commonly seen for ion mill etchings. Therefore, a thick photoresist mask is required to prevent this tapered profile being transferred into LN. Finally, we pattern a 80nm thick top gold electrode using lift-off and the devices are released in BOE 6:1, and dried in critical point dryer (CPD).

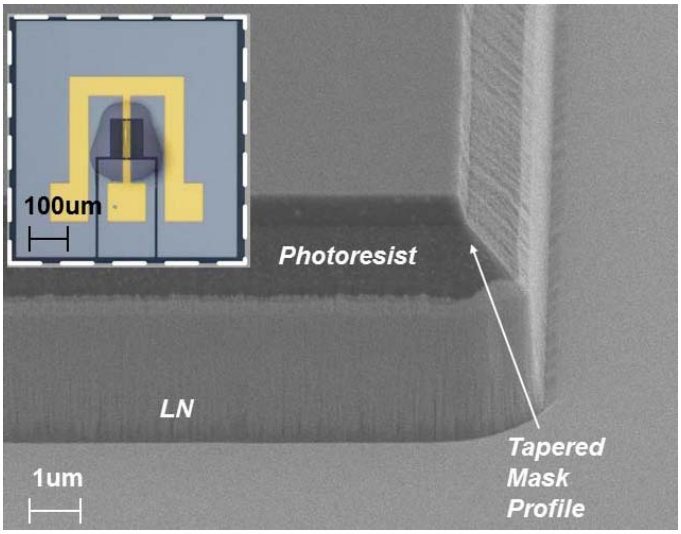


Fig. 4. SEM of side-wall profile of lithium niobate and photoresist mask after ion-mill etching; the inset shows the microphotograph of one finished device.

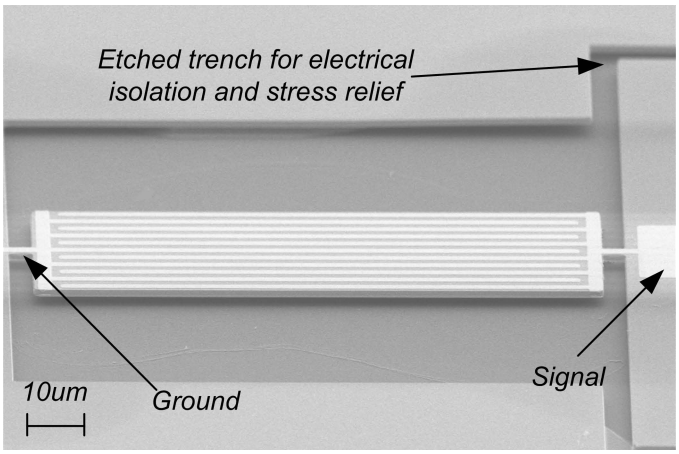


Fig. 5. SEM of a 97um × 39.6um LN $S_0$ Lamb wave mode resonator with 11 finger electrodes.

It is worth noting that the bonding and thinning process unavoidably adds stress which can build up at anchors during timed release process. Ion-milled trenches around the signal pad isolate the anchor bases, thereby providing stress relief and reducing parasitic capacitive feed-through (Fig. 4 inset). Fig. 5 is the SEM of the released device imaged at a 70 degree incident angle indicating that the structure has no evidence of buckling or bowing.

## III. Design and Modeling

The resonator consists of a block of free-standing thin-film LN with IDTs on top. When an RF potential is applied to the fingers, it generates periodic strains in the lateral direction from the piezoelectric effect. Because of the discontinuity at the boundaries of the LN block and the IDT fingers, only certain mechanical modes of vibration can fit in the resonator. As a result, only an RF signal that can excite these particular modes can excite resonance in the system. As the length of the devices is generally much longer than the width, the resonant frequency can be approximately expressed as:

$$f = m \times \frac{v_{acoustic}}{W} \tag{1}$$

where $W$ is the width of the resonator, $m$ is the mode order of the vibration, and $v_{acoustic}$ is the velocity of $S_0$ Lamb wave in the LN thin-film. Therefore, the resonant frequency can be defined through the width of the device.

### A. Electrode Configuration Trade-Offs

The IDT configuration has significant impact on many aspects of the performance of LN $S_0$ Lamb wave mode resonators. First of all, the mass loading effect from the electrodes can shift the resonator frequency, while the scattering of acoustic wave by acoustic-impedance mismatched electrodes, acoustic loss of the electrode material, and the interfacial loss can degrade the quality factor. Second, the metallization ratio and electrode location with respect to the mechanical mode affects the overlap integral between the excitation field profile and the mechanical mode profile, therefore affects coupling of targeted mode of operation. Finally, the relative phase of scattering from electrodes and device boundaries can lead to resonance at undesired parasitic modes. Here, we discuss the resonator performance from two different kinds of electrode placement, namely the type with electrodes placed at mechanical anti-nodes (AN type) and the type with electrodes placed at the mechanical nodes (N type). A detailed analytical model for behavior of the IDT can be found in [17] but we provide an intuition for different IDT designs.

Optimum $k_{eff}^2$ for y-136 LN is realized by exciting the $S_0$ Lamb mode using IDT placed on the top surface, while the location of the electrodes plays an essential role on the performance of the resonator. Fig. 6 shows the cross-section of resonators with the AN type and N type electrode. The total width of the resonator is $N\lambda/2$. Both electrode configurations have a metallization ratio of 0.5, $\lambda/4$ finger pairs, and a period of $\lambda/2$. However the AN type has two $\lambda/8$ fingers right at the edges of the device. For a SAW device, the IDT has a frequency response of sinc function [18]. However, the sharply defined mechanical boundaries of the Lamb wave resonator form an equivalent mechanical Fabry-Perot (FP) cavity. Therefore, the IDT for Lamb wave resonator has a frequency response of sinc function combined with the frequency response of the FP cavity. For the AN type, the boundary conditions from the device geometry coincides with that from the electrode finger centers. Therefore, the two sets of boundary conditions both reinforce the mechanical mode defined by the wavelength of $\lambda$ (Fig. 6(b)). In contrast, the boundary conditions are offset for the N type. Thus, the mode corresponding to $\lambda$ is extinguished, while the next lower order mode (Fig. 6(c)) and the next higher order mode (Fig. 6(d)) are excited. Fig. 7 shows the admittance of a N type resonator and an AN type resonator simulated in COMSOL. The simulated $N$ and $\lambda$ for both resonators are 5 and $7.6um$. The AN type has one main resonance at 762MHz corresponding to the $5^{th}$ order $S_0$ mode, while the other spurious harmonic modes are suppressed by greater than 10dB. The corresponding mode

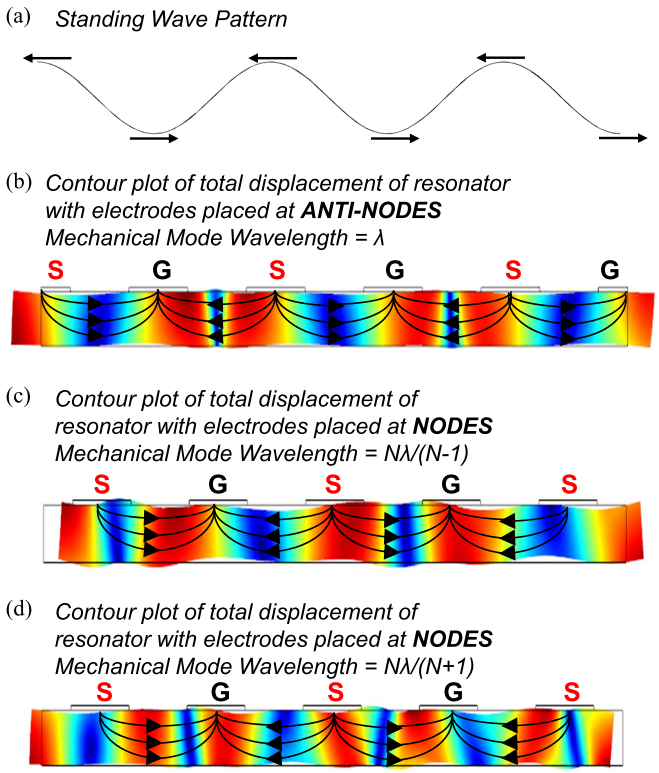


Fig. 6. Cross-section of resonators on y-136 LN with electrodes placed at anti-nodes and electrodes placed at nodes, the crystal x-axis is pointing out of the paper. The COMSOL simulated contour plots show the total displacement of different order modes with black arrows pointing the direction of E-field. (a) The standing wave pattern (arrows pointing the direction of displacement) of the $N^{th}$ order mode ($5^{th}$) with a wavelength of $\lambda$, (b) Deformation of the $N^{th}$ order mode ($5^{th}$) with electrodes place at anti-nodes, (c) Deformation of the mode with a wavelength of $N\lambda/(N-1)$ (electrodes placed at nodes), (d) Deformation of the mode with a wavelength of $N\lambda/(N+1)$ (electrodes placed at nodes).

shapes of the spurious modes are identified in Fig. 7, which indicates that these spurs are $S_0$ Lamb wave modes. The N type IDT does not couple to the $5^{th}$ order mode. Instead, it couples to the $2^{nd}, 4^{th}, 6^{th}, 8^{th}, ...$ even order modes. The excitation of $S_0$ mode on y-136 cut LN is primarily through the $d_{22}$ coefficient, which is almost four times larger than the $d_{33}$ coefficient of AlN. Therefore, spurious $S_0$ modes can be easily excited with improper IDT designs. It is worth noting that the $8^{th}$ order mode for the N type device exhibits $A_0$ mode like features because of its degeneracy with a high order $A_0$ mode.

The excitation E-field profile from the AN type electrodes has a better overlap with the excited mechanical mode, while the overlap is reduced for N type because of the shift of electrode with respect to the device boundaries (This can be observed by comparing the mode deformation and the electric field pattern for the $N\lambda/(N-1)$ in Fig. 6). Consequently, the AN type will also exhibit better $k^2_{eff}$ comparing to the N type. However, the drawback of the AN type is that electrodes cause stronger acoustic scattering, because of the large displacement at the mechanical anti-nodes.

### *B. Displacement and Vacuum Testing*

Because of the high coupling coefficients and relatively small elasticity coefficients, a small RF power can cause large displacement from LN resonator. A $-12$dBm RF drive power is sufficient to cause $>1nm$ displacement in the propagation direction of the acoustic wave, while the AlN counterparts moves 50 times less. The displacement from LN resonator is within one order of magnitude of air mean-free-path in room pressure (70nm), putting the device quality factor in the air damping limited regime at room pressure.

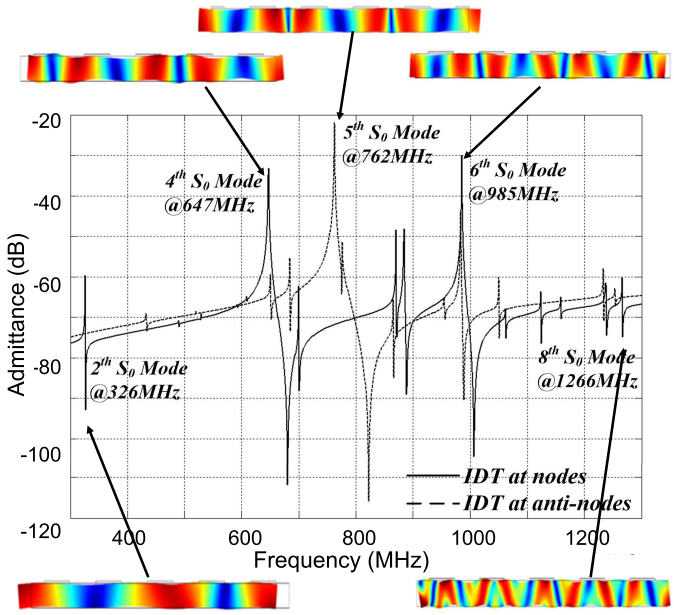


Fig. 7. Admittance and deformation of $S_0$ Lamb wave modes of resonators with IDT at anti-nodes and at nodes simulated in COMSOL.

## IV. Experimental Results

The performance of the 1-port resonators are measured with an E8364B vector network analyzer, where a $-16$dBm stimulus is used. We calculate the quality factor from the raw data using the method described in [19]. To better estimate the $k^2_{eff}$, the parasitic feed-through pad capacitance is de-embedded by measuring open structures with only the probe pads [20] (The de-embedding process only cancels the parastic capacitance, and does not cancel any series routing resistance). For the devices presented in this paper, the parasitic feed-through capacitance is $63.8\,fF$. The effective $k^2_{eff}$ is calculated using the following definition:

$$k^2_{eff} = 1 - (\frac{f_s}{f_p})^2 \tag{2}$$

where, $f_s$ and $f_p$ are the frequencies of the series and parallel resonant peaks.

### *A. Quality Factor vs. Pressure*

Fig. 8 shows the measured admittance (magnitude and phase) of the $6^{th}$ order mode of a 462MHz "N type IDT" resonator in air and vacuum ($5.4 * 10^{-3}$ mbar). The device design parameters are shown in Table I. The phase transition of the device shows a clean swing from $+90°$ to $-90°$. The impedance ($R_s$) at the series peak is 51 Ohm in air and 36.5 Ohm in vacuum, with a $k^2_{eff}$ of 7%. The quality

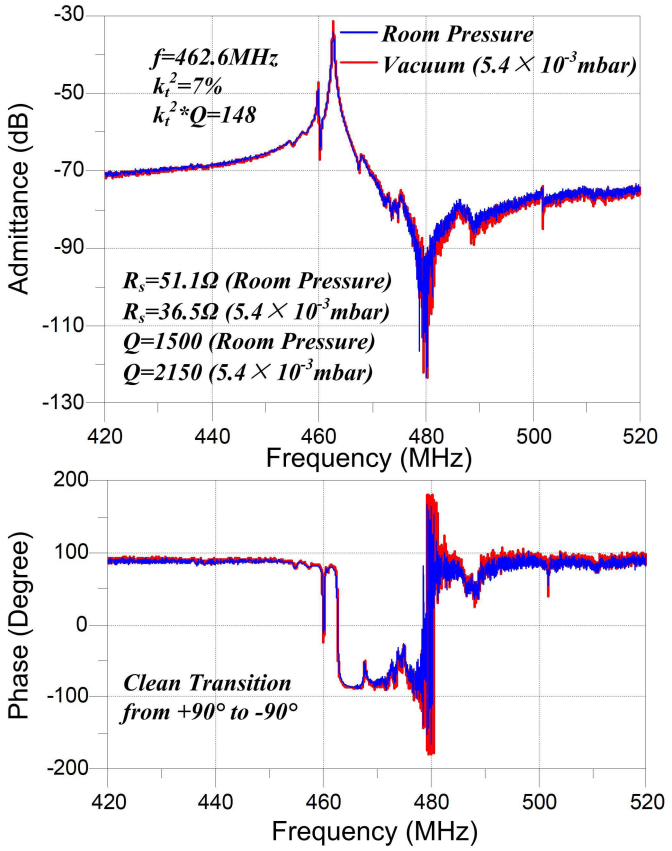


Fig. 8. Measured admittance (after de-embedding the parasitic capacitance) of a 462MHz "N type IDT" resonator measured in vacuum and air. MilliTorr vacuum improves the $Q$ by 30%, resulting in the FOM of 148, which surpasses that of AlN CMRs.

TABLE I
DESIGN PARAMETERS OF THE 462MHZ N TYPE IDT RESONATOR

| No. of Fingers | IDT Width | N | $\lambda$ | Total Width $(N * \lambda/2)$ |
|---|---|---|---|---|
| 7 | $2.8um$ | 7 | $11.2um$ | $39.2um$ |

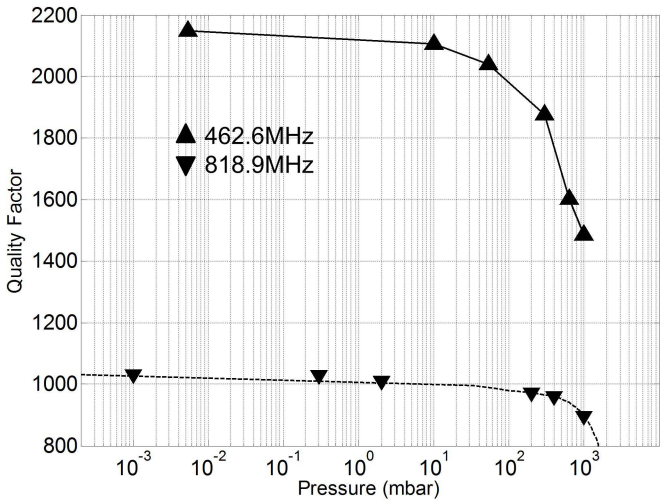


Fig. 9. $Q$ of the 462MHz resonator and the 818.9MHz resonator as a function of pressure showing evidence of air damping.

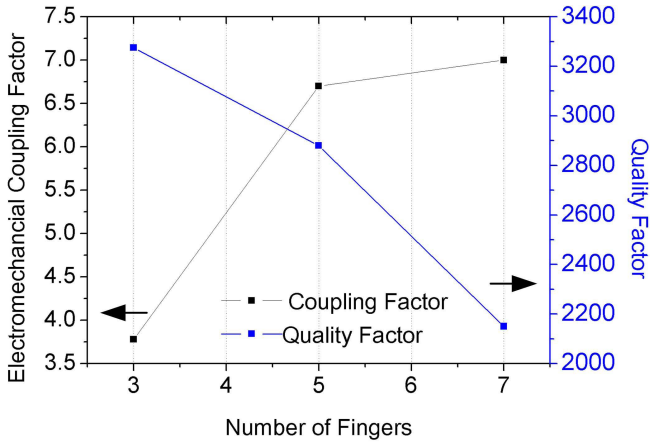


Fig. 10. $Q$ and $k_{eff}^2$ as function of number of electrode fingers.

factor of the series peak is 1500 in air, comparing to 2150 in vacuum. The improvement in $Q$ arises from reduction of air damping in vacuum. To further verify the device is air damping limited, we measured $Q$ versus pressure which exhibits clear signature of air damping (Fig. 9). This $Q$ improvement from air to vacuum, along with the 7% $k_{eff}^2$ results in a $k_{eff}^2 \times Q$ of 148. Also, Fig. 9 shows the $Q$ of a 818.9MHz device as a function of pressure. The $Q$ goes from 890 to 1030, improved by 15% going from room pressure to vacuum. The reduced improvement of $Q$ is expected, since the displacement is less going to higher frequency.

### *B. Electrode Loading of Quality Factor*

Ideally, the electrode material should have low internal losses and an acoustic impedance that is matched to LN for high $Q$ operation. However, gold, notorious for high internal friction [21], is used here because of process compatibility issues. Therefore, the impact on the mechanical quality factor of the resonators due to loss from the metal electrode is investigated. Fig. 10 shows the $Q$ and $k_{eff}^2$ as a function of number of fingers for the $6^{th}$ order mode of three devices. The three devices has the same design as the one shown in table I, except that the outer most 2 fingers are subsequently removed for resonators with decreasing number of finger electrodes (Fig. 11). $Q$ of these devices increases from 2150 to 3300 as the number of finger number decreases from 7 to 3, which indicates that the $Q$ is dominated by loss from the electrodes. The function is not linear suggesting another loss mechanism starts to limit the $Q$ as the finger number decreases. The coupling factor reduces with finger number from 7% to 3.7%, since less energy is coupled with decreasing number of electrodes. The quality factor of the device with only 3 finger electrodes is 3300 at 498.3MHz, yielding a $f \times Q$ of $1.6 \times 10^{12}$. This is only one order of magnitude less than the phonon-phonon interaction limited $f \times Q$ of bulk LN [22]. Moreover, the $k_{eff}^2 \times Q$ of the device with 5 fingers is 194 where the $k_{eff}^2$ and $Q$ are 6.8% and 2850.

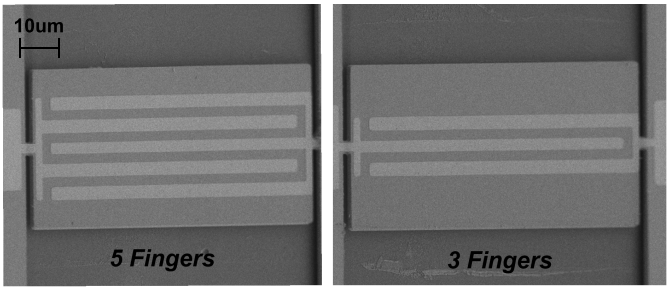


Fig. 11. SEM of lithium niobate resonators with 5 electrode fingers and 3 electrode fingers respectively.

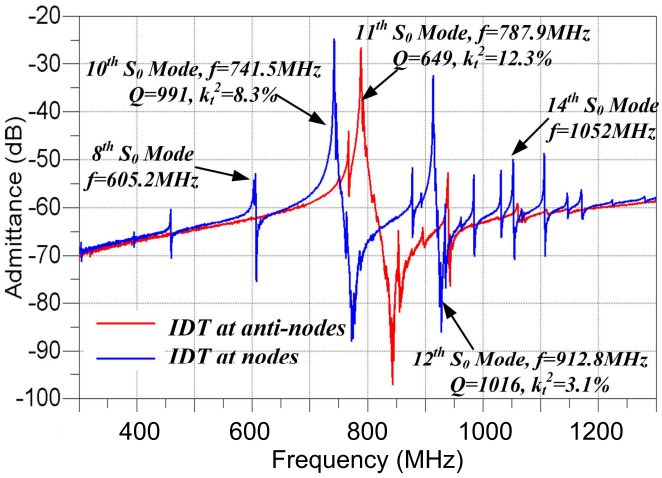


Fig. 12. Measured admittance of the two configurations in vacuum. While the N type configuration has higher series Q, the anti-node configuration has significantly fewer spurs and exceptional coupling coefficient.

TABLE II
DESIGN PARAMETERS OF MULTI-FREQUENCY $S_0$ LAMB WAVE RESONATORS

| | No. of Fingers | Finger Width | N | $\lambda$ | Total Width $(N*\lambda/2)$ |
|---|---|---|---|---|---|
| Fig. 12 | 11 | $1.8um$ | 11 | $7.2um$ | $39.6um$ |
| Fig. 13 | 7 | $2.8um$ | 7 | $11.2um$ | $39.2um$ |
| Fig. 13 | 9 | $2.8um$ | 9 | $11.2um$ | $50.4um$ |
| Fig. 14 | 11 | $1.4um$ | 11 | $5.6um$ | $30.8um$ |

### C. Multi-Frequency Resonators

Fig. 12 shows the measured admittance (in vacuum) of an AN type resonator and a N type resonator. The total widths of both devices are $11/2\lambda$, where $\lambda$ is 7.2um (Table II). As predicted in Section II.A, the AN type device only shows one main peak at 787.9 MHz, which corresponds to $11^{th}$ order mode with the 7.2 um wavelength. The device shows an excellent $k^2_{eff}$ of 12.3% and significantly fewer spurs. However, the Q is 650, lower than the N type because of the acoustic scattering caused by the electrodes. In comparison, the N type configuration shows two strong resonance peaks corresponds to the modes with wavelengths of $N\lambda/(N-1)$ and $N\lambda/(N+1)$, which matches our modeling. The frequencies of the two modes are 741.5 MHz and 912.8 MHz. Both

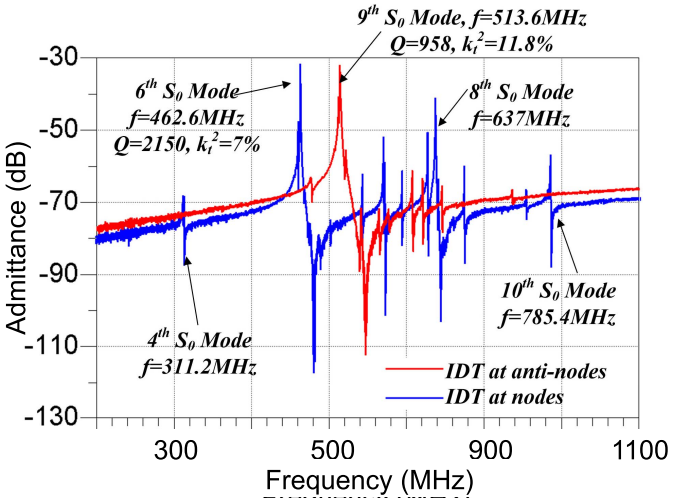


Fig. 13. Measured admittance of the AN and N type resonators with wavelength of $11.2um$.

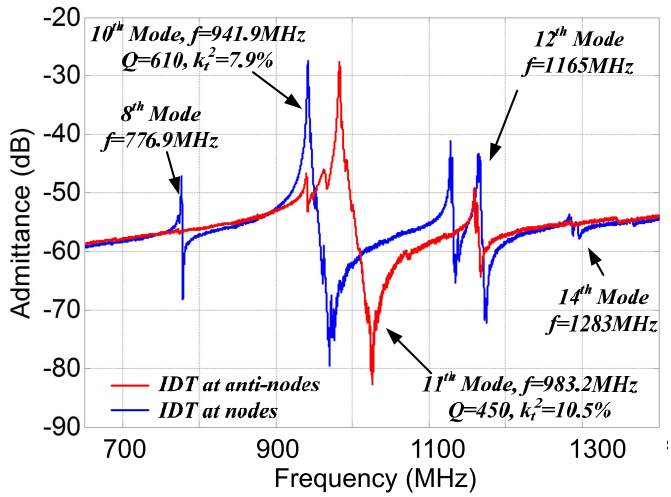


Fig. 14. Measured admittance of the AN and N type resonators with wavelength of $5.6um$.

modes show high $Q$ of ~1000. The $k^2_{eff}$ of the 741 MHz mode is 8.3%, and the $k^2_{eff}$ of the 912.8 MHz is 3.1%, which is caused by the smaller overlap between the excitation field and mechanical mode profile. Ideally, the $(N-1)$ mode should have a frequency of $(N-1)f_0/N$, where N is the total periods of the device and $f_0$ is the frequency of the main resonant peak of the AN type. However, the measured frequencies of the N type are higher than that predicted by the simple first-order theory. This is because of the mechanical dispersion, and the mass loading from the electrode is less for the N type devices as compared to the AN type.

Similarly, Fig. 13 shows the AN and N type devices with the same wavelength of 11.2um, where the N type has a total period of 7 and the AN type has a total period of 9. Once again, the N type IDT excites the next lower and next higher order modes ($6^{th}$ and $8^{th}$), instead of the $7^{th}$ order mode; while the AN type only strongly excites the $9^{th}$ order mode. This proves that the distinct responses of the two types of devices indeed originate from the relative location of electrodes,

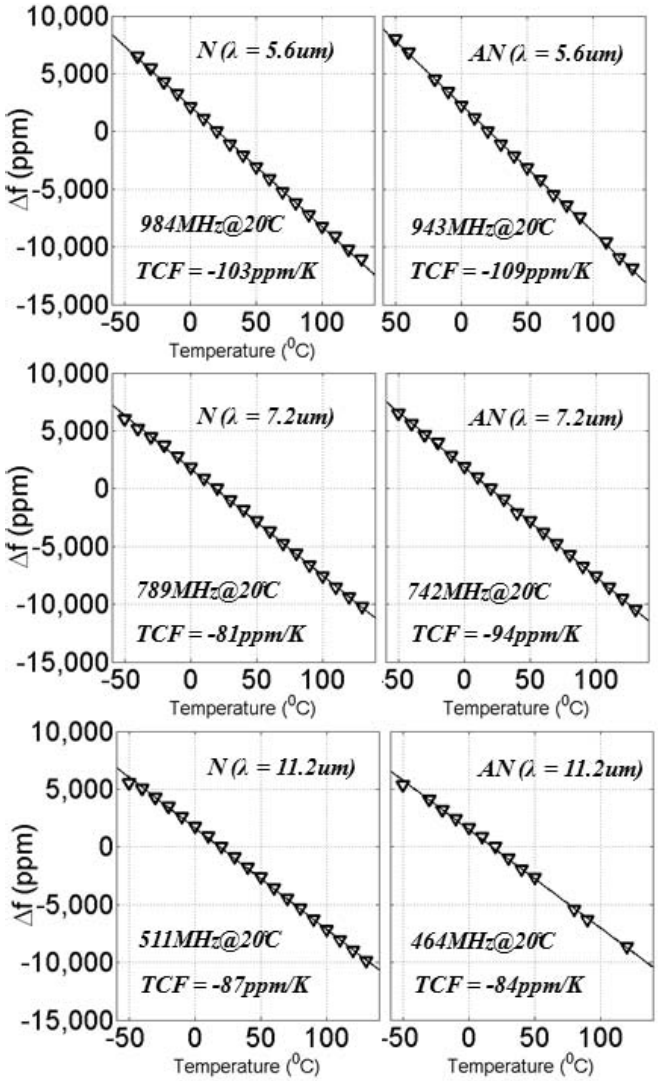


Fig. 15. Measured TCF of LN resonators with different wavelengths and different electrode configurations.

not from the total number of periods of the resonators. The N type has higher $Q$ (2150 for the $6^{th}$ order mode and 2500 for the $8^{th}$ order mode) and lower coupling factor (7% for the $6^{th}$ order mode and 2.1% for the $8^{th}$ order mode), while the AN type has higher coupling factor (11.8%) and lower $Q$ (958). Finally, Fig. 14 shows the devices designed to operate near 1GHz series resonant frequency. The $11^{th}$ order mode of the AN type has a $k_{eff}^2$ and $Q$ of 10.5% and 450, while the $10^{th}$ order mode of the N type has a $k_{eff}^2$ and $Q$ of 7.9% and 610.

### D. Temperature Stability

The temperature coefficient of frequency (TCF) of both the AN type and the N type resonators with diferent wavelengths are measured by sweeping the temperature from −50°C to 130°C. As shown in Fig. 15, the TCFs range from −84ppm/K to −109ppm/K. This is consistent with the TCF of a typical LN SAW filter without temperature compensation. While the TCFs are larger than AlN FBARs, temperature compensation using silicon dioxide compensation layer has been investigated [23], [24].

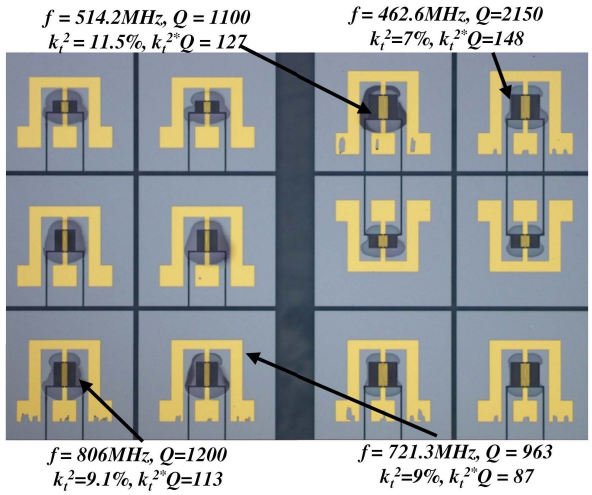


Fig. 16. Microphotograph of one corner of a single chip, on which device resonances are defined at different frequencies by photolithography.

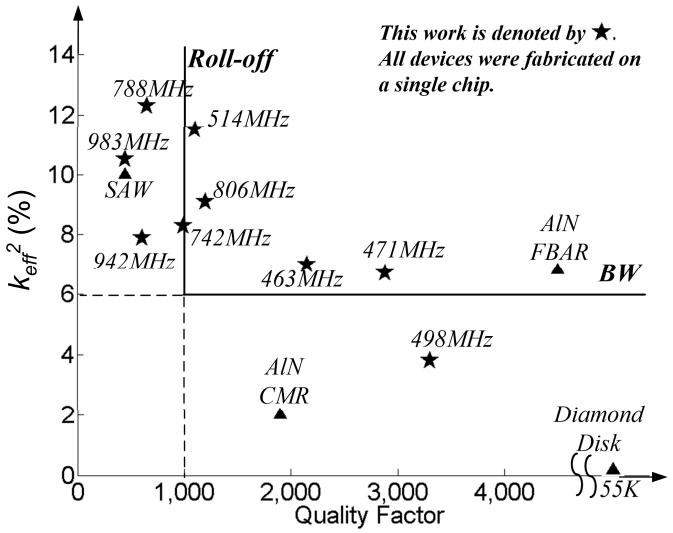


Fig. 17. Electromechanical coupling factor vs quality factor (measured in vacuum). Comparison of this work to current state of art.

### E. Comparison to Other Resonator Technologies

By employing different electrode configurations and using different device dimensions, we were able to demonstrate resonators with different frequencies, quality factors and $k_{eff}^2$. Fig. 16 shows a microphotograph of one corner (2.4mm × 1.9mm) of a single chip. At the upper right corner, the two devices have a wavelength of 11.2um. The resonant frequency for the AN type is 514.2MHz with a $Q$ of 1100 and $k_{eff}^2$ of 11.5%, while the N type shows lower resonant frequency and $k_{eff}^2$, but higher $Q$. Similarly, the lower left corner shows two devices with wavelength of 7.2 um. Fig. 17 summarizes measured performance (in vacuum) of different devices manufactured on a single chip. The resonant frequencies range from 463 MHz to 983 MHz, while the highest $k_{eff}^2$ achieved on this chip is 12.3%. The quality factor measured in vacuum ranges from 700 to 3300. The highest $k_{eff}^2 \times Q$ achieved on this chip is 194. Comparing to other technologies, our resonators show sufficient quality

factor to achieve fast roll-off comparable to traditional MEMS resonators, meanwhile provides much higher $k^2_{eff}$ for wide BW operation. In addition, the great versatility of our devices will facilitate single chip integration of devices with different frequencies.

## V. Conclusion

In this work, we present the fabrication technology and design of $S_0$ Lamb wave mode thin-film $LiNbO_3$ resonators that can enable multi-frequency, wide bandwidth, low insertion loss and fast roll-off filters. We focused on the design of the interdigital transducer and its impact on the performance of the resonator. We identify that losses from the metal electrodes are the key limiting mechanism of $Q$, and investigate the TCFs of these devices. With the flexibility of IDT configuration and lithography-defined resonator geometry, we demonstrated resonators with a wide range of performance on a single chip. The $k^2_{eff} \times Q$ goes up to 194, $k^2_{eff}$ and $Q$ as high as 12.3% and 3300. For RF filters, the $k^2_{eff}$ and $Q$ leads to wide bandwidth, steep roll-off and low insertion loss. Comparing to other technologies (Fig. 17), we can achieve both high $Q$ and high $k^2_{eff}$, and more importantly provide the flexibility to integrate multi-frequency resonators and filters on a single chip.

## Acknowledgment

They would also like to thank Dr. Seungbae Lee, Professor Sheng-Shian Li, Dr. Warren Welch, and Dr. Jason Reed for initial work on LN resonator and process development.

## References

[1] J. Wang, J. E. Butler, T. Feygelson, and C. T.-C. Nguyen, "1.51-GHz nanocrystalline diamond micromechanical disk resonator with material-mismatched isolating support," in *Proc. IEEE Int. Conf. Micro Electro Mech. Syst. (MEMS)*, Jan. 2004, pp. 641–644.

[2] R. Ruby *et al.*, "Positioning FBAR technology in the frequency and timing domain," *IEEE Trans. Ultrason., Ferroelectr., Freq. Control*, vol. 59, no. 3, pp. 334–345, Mar. 2012.

[3] C.-M. Lin, Y.-Y. Chen, V. V. Felmetsger, D. G. Senesky, and A. P. Pisano, "AlN/3C—SiC composite plate enabling high-frequency and high-$Q$ micromechanical resonators," *Adv. Mater.*, vol. 24, no. 20, pp. 2722–2727, May 2012.

[4] G. Piazza, P. J. Stephanou, J. P. Black, R. M. White, and A. P. Pisano, "Single-chip multiple-frequency RF microresonators based on aluminum nitride contour-mode and FBAR technologies," in *Proc. IEEE Int. Ultrason. Symp. (IUS)*, vol. 2. Sep. 2005, pp. 1187–1190.

[5] M. Kadota, T. Kimura, and Y. Ida, "Ultra wide band resonator composed of grooved Cu-electrode on $LiNbO_3$ and its application to tunable filter," in *Proc. IEEE Int. Ultrason. Symp. (IUS)*, Sep. 2009, pp. 2668–2671.

[6] R. Wang, S. A. Bhave, and K. Bhattacharjee, "High $kt^2 \times Q$, multi-frequency lithium niobate resonators," in *Proc. 26th IEEE Int. Conf. Micro Electro Mech. Syst. (MEMS)*, Jan. 2013, pp. 165–168.

[7] R. H. Olsson *et al.*, "A high electromechanical coupling coefficient $SH_0$ Lamb wave lithium niobate micromechanical resonator and a method for fabrication," *Sens. Actuators A, Phys.*, vol. 209, pp. 183–190, Mar. 2014.

[8] S. Gong and G. Piazza, "Figure-of-merit enhancement for laterally vibrating lithium niobate MEMS resonators," *IEEE Trans. Electron Devices*, vol. 60, no. 11, pp. 3888–3894, Nov. 2013.

[9] C.-M. Lin, V. Yantchev, J. Zou, Y.-Y. Chen, and A. P. Pisano, "Micromachined one-port aluminum nitride Lamb wave resonators utilizing the lowest-order symmetric mode," *J. Microelectromech. Syst.*, vol. 23, no. 1, pp. 78–91, Feb. 2014.

[10] H. Akazawa and M. Shimada, "Electron cyclotron resonance plasma sputtering growth of textured films of c-axis-oriented $LiNbO_3$ on Si(100) and Si(111) surfaces," *J. Vac. Sci. Technol. A, Vac., Surf., Films*, vol. 22, no. 4, pp. 1793–1798, Jul. 2004.

[11] S. Tan, T. Gilbert, C.-Y. Hung, T. E. Schlesinger, and M. Migliuolo, "Sputter deposited c-oriented $LiNbO_3$ thin films on $SiO_2$," *J. Appl. Phys.*, vol. 79, no. 7, pp. 3548–3553, Apr. 1996.

[12] R. A. Betts and C. W. Pitt, "Growth of thin-film lithium niobate by molecular beam epitaxy," *Electron. Lett.*, vol. 21, no. 21, pp. 960–962, Oct. 1985.

[13] M. Kadota, T. Ogami, K. Yamamoto, H. Tochishita, and Y. Negoro, "High-frequency Lamb wave device composed of MEMS structure using $LiNbO_3$ thin film and air gap," *IEEE Trans. Ultrason., Ferroelectr., Freq. Control*, vol. 57, no. 11, pp. 2564–2571, Nov. 2010.

[14] A. Guarino, G. Poberaj, D. Rezzonico, R. Degl'Innocenti, and P. Günter, "Electro–optically tunable microring resonators in lithium niobate," *Nature Photon.*, vol. 1, pp. 407–410, Jul. 2007.

[15] S. Benchabane, L. Robert, J.-Y. Rauch, A. Khelif, and S. Laude, "Highly selective electroplated nickel mask for lithium niobate dry etching," *J. Appl. Phys.*, vol. 105, no. 9, pp. 094109-1–094109-6, 2009.

[16] H. Hui, R. Ricken, and W. Sohler, "Etching of lithium niobate: From ridge waveguides to photonic crystal structures," in *Proc. Eur. Conf. Integr. Opt.*, 2008, pp. 75–78.

[17] R. Wang, S. A. Bhave, and K. Bhattacharjee, "Modeling of inter-digitated transducer for high-order contour mode resonators," in *Proc. IEEE Int. Ultrason. Symp. (IUS)*, Jul. 2013, pp. 1926–1929.

[18] M. Kadota, J. Ago, H. Horiuchi, and M. Ikeura, "Very small IF resonator filters using reflection of shear horizontal wave at free edges of substrate," *IEEE Trans. Ultrason., Ferroelectr., Freq. Control*, vol. 49, no. 9, pp. 1269–1279, Sep. 2002.

[19] D. A. Feld, R. Parker, R. Ruby, P. Bradley, and S. Dong, "After 60 years: A new formula for computing quality factor is warranted," in *Proc. IEEE Int. Ultrason. Symp. (IUS)*, Nov. 2008, pp. 431–436.

[20] D. M. Pozar, *Microwave Engineering*. Hoboken, NJ, USA: Wiley, 2011.

[21] C. Zener, "Internal friction in solids. I. Theory of internal friction in reeds," *Phys. Rev.*, vol. 52, pp. 230–235, Aug. 1937.

[22] M. Pijolat *et al.*, "Large $Q \times f$ product for HBAR using smart cut transfer of $LiNbO_3$ thin layers onto $LiNbO_3$ substrate," in *Proc. IEEE Int. Ultrason. Symp. (IUS)*, Nov. 2008, pp. 201–204.

[23] L. Shi and G. Piazza, "Ion-sliced lithium niobate on silicon dioxide for engineering the temperature coefficient of frequency of laterally vibrating resonators," in *Proc. Joint Eur. Freq. Time Forum Int. Freq. Control Symp. (EFTF/IFC)*, Jul. 2013, pp. 417–420.

[24] C.-M. Lin *et al.*, "Temperature-compensated aluminum nitride Lamb wave resonators," *IEEE Trans. Ultrason., Ferroelectr., Freq. Control*, vol. 57, no. 3, pp. 524–532, Mar. 2010.

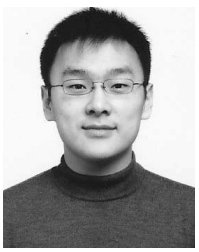

**Renyuan Wang** received the B.S. degree from the Harbin Institute of Technology, Harbin, China; the M.S. degree in electrical engineering from the University of Massachusetts at Dartmouth, Dartmouth, MA, USA; and the Ph.D. degree in electrical and computer engineering from Cornell University, Ithaca, NY, USA, where he is currently a Post-Doctoral Researcher. He worked in developing high-dynamic coherent photonic RF radar front-ends. He is involved in lithium niobate thin-film devices on the application of RF MEMS, optomechanics, nonlinear optics, and inertial measurement units.

**Sunil A. Bhave** received the B.S. and Ph.D. degrees in electrical engineering and computer science from the University of California at Berkeley, Berkeley, CA, USA, in 1998 and 2004, respectively.

Since 2004, he has been with Cornell University, Ithaca, NY, USA, where he is currently an Associate Professor with the School of Electrical and Computer Engineering. His research interests include exploring, understanding, and exploiting interdomain coupling in optomechanical, spin-acoustic, and atom-MEMS systems to design inertial sensors, clocks, and field-programmable microwave chipsets.

Dr. Bhave was a recipient of the National Science Foundation Early CAREER Development Award in 2007, the Defense Advanced Research Projects Agency Young Faculty Award in 2008, and the IEEE Ultrasonics Young Investigator Award in 2014. Along with his students, he has been awarded the Roger A. Hakan Best Paper Award at the International Electron Devices Meeting in 2007, and the Student Paper Competition Award at the IEEE International Ultrasonics Symposium in 2009 and the IEEE Photonics Conference in 2012.

**Kushal Bhattacharjee** received the M.S. degree in physics from IIT Delhi, New Delhi, India; the M.S.E.E. degree from Rensselaer Polytechnic Institute, Troy, NY, USA; and the Ph.D. degree in electrical engineering from the University of Connecticut, Storrs, CT, USA. Prior to joining as a Principal Engineer in RF Micro Devices, Inc., in Greensboro, NC, USA, in 2004, he worked in design and research and development areas in various companies, including Andersen Laboratories, Auburn, NY TRW Space and Defense, Euclid, OH, USA; and Motorola, Chicago, IL, USA. His professional interests include filter and frequency controlling technology development, SAW and bulk acoustic wave devices, and piezoelectric MEMS.